Experimental investigation of swirl number influence on spiral vortex structure dynamics

D Štefan[1], M Hudec[1], V Uruba[2], P Procházka[2], O Urban[1], P Rudolf[l]

[1] V. Kaplan Department of Fluid Engineering, Faculty of Mechanical Engineering, Brno University of Technology, Technická 2896/2, 61699 Brno, Czech Republic
[2] Institute of Thermomechanics, The Czech Academy of Science, Dolejškova 1402/5, Prague, Czech Republic

E-mail: stefan@fme.vutbr.cz

Abstract. The hydraulic turbines are recently forced to operate far away from the optimal conditions in order to balance fluctuations in electricity generation. In case of Francis, pump and propeller turbines, using only single control component of guide vanes, it means that in regions where the high residual swirl enters the draft tube, the flow is decelerated and convenient conditions for the vortex rope development are created. Such flow conditions are considered to be the triggering mechanism for occurrence of different forms of vortex structures in the Francis turbine draft tube, e.g. spiral or straight vortex rope at part load or full load respectively. Independently on the vortex rope shape the unsteady pressure fields develop producing periodic stress on turbine components and possibly resulting in noise, blade cracks, runner lift, power swing, etc. To study and mimic such flow conditions, a simplified device of vortex generator apparatus is employed. Thanks to its design, the vortex generator enables to change the ratio between fluxes of axial momentum and tangential moment of momentum of generated swirl. Then, the behavior of vortex structure changes in a similar way as the flow rate variation in the draft tube of Francis turbine. For above mentioned reasons the unsteady cavitating spiral vortex is experimentally studied using both high speed video record and particle image velocimetry (PIV). The main focus is on change of vortex dynamics regarding to the swirl number variation. The proper orthogonal decomposition (POD) together with the classical fast Fourier transformation (FFT) are employed to extract dominant modes and frequencies from experimental data.

1. Introduction

The spiral vortex (special form of so called "vortex rope" in hydro-turbine terminology) is one of the main flow structures found in the draft tube (outlet diffuser) of Francis turbine operated at part load. At part load the flow rate Q is lower than one at the best efficiency point Q_{BEP} and the high residual swirl exits the turbine outlet and enters the draft tube where the remaining kinetic energy is transformed to the static pressure. This decelerated swirling flow tends to be unstable, thus the highly unsteady pressure field with the spiral vortex rotating around 25% of the runner speed is formed. The resulting high pressure amplitudes strain the mechanical parts of the turbine (e.g. blades, bearings) [1], cause power swing in electricity generation [2, 3, 4] and produce significant mechanical noise. For this reason it is important to understand the main source of dominant frequencies which could also cause resonance of some parts in hydraulic system [5]. In order to study dynamical behavior of such vortex structure the simplified approach

consisting of swirling apparatus was employed in several researchers' studies [6, 7, 8, 9, 10, 11] and various spiral vortex behaviors were reported: transition from single to twin spiral vortex [12, 13], self-oscillating vortex rope dynamic of synchronous character [14, 15] and finally the vortex re-connection with formation of vortex rings [16, 17, 18, 19].

It is important to understand all these mentioned instabilities since the hydraulic turbines are forced to operate far away from the optimal conditions in order to balance fluctuations in electricity generation. For this reason the simplified device of swirl generator was used to study changes in vortex dynamics regarding to the swirl number variation.

2. Swirl generator

The vortex generator presented in this study was developed with aim to change the ratio between fluxes of axial momentum and tangential moment of momentum of generated swirl. Such a geometry enables to adjust the swirl parameters while keeping the simple design for manufacturing and operation (e.g. exclude any rotating parts). This was ensured by the inflow separated to axial and tangential entrance. The tangential inflow Q_t is mixed with axial one Q_a using the spiral geometry without any blade cascade. The swirl generator geometry is shown in figure 1 where the red plane marks longitudinal cross-section in axial direction and blue plane the mid-cross-section in the spiral. This swirl generator was already used in several numerical [20, 21] and experimental studies [19].
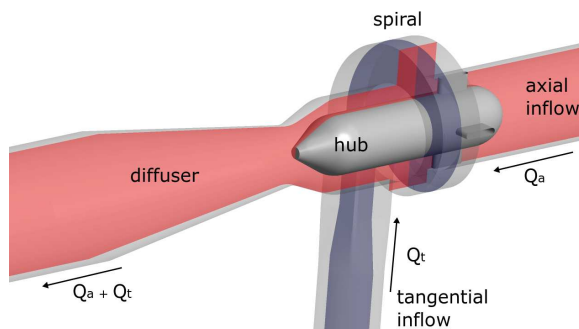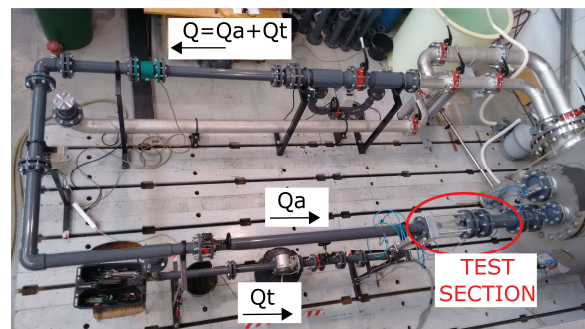

Figure 1. Geometry of swirl generator.

Figure 2. Test rig overview.

3. Measurements

Measurements were performed using the closed loop hydraulic circuit where the water is supplied by the pump situated in the basement of laboratory. For both axial Q_a and tangential Q_t inflow the static pressure level and flow rate were measured. The photo of test-rig with installed swirl generator is shown in figure 2.

This paper presents results of two experimental campaigns. While the first one was concentrated on visual observation of cavitating vortex using the high speed camera (HSC), the second one employed stereoscopic particle image velocimetry (S-PIV) to obtain information about velocity distribution in longitudinal planes situated within transparent diffuser. Assuming the diffuser throat diameter $D_t = 0.05$ m as a reference length the Reynolds number for nominal flow rates $Q_n = 10$ l/s and $Q_n = 5$ l/s is $Re = 254647$ and $Re = 127323$, respectively.

3.1. High speed camera recording
For the image recording of cavitating vortex the high speed camera Ximea CB120MG-CM-X8G3 was used. This camera, consisting of 12 MPx monochrome CMOSIS sensor, was equipped with Canon EF 50 mm f/1.4 USM lens characterized by a very good aperture and focal length without image distortion. For the scene illumination the 238 x 190 mm large LED lightening panel

Aputure Amaran HR consisting of 672 LED bulbs was used. In order to record vortex structure filled with the water vapors, the so called back-light method was employed as suitable and previously proved technique. According to the layout shown in figure 3 the camera, light source and recorded object are situated inline. While the camera is heading towards the light source, the recorded object is in the middle of the scene. In our case the diffuser was manufactured from acrylic glass, thus it is fully transparent. The LED panel was placed just aside the diffuser wall and camera was placed approximately in distance of 0.5 m. The final record was done with aperture F2.5 and frame rate 1487.5 fps.
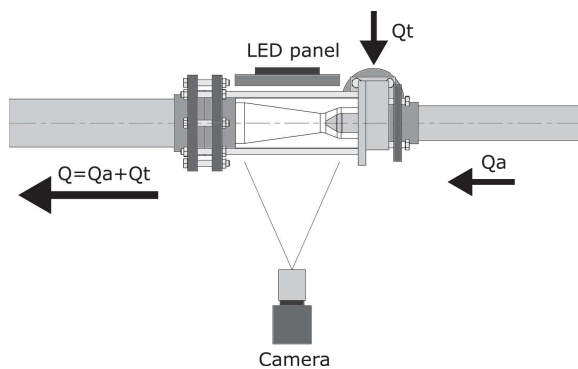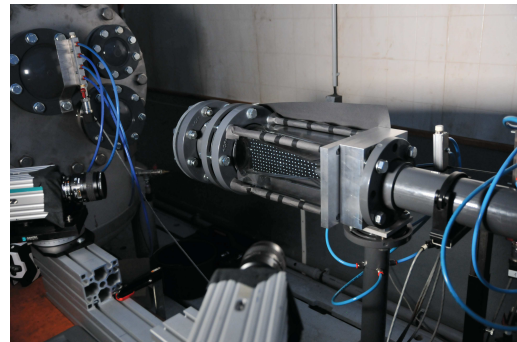

Figure 3. Layout of HSC recording.

Figure 4. S-PIV calibration arrangement for longitudinal target.

3.2. PIV measurements
The stereoscopic PIV (S-PIV) measurements were done employing the Pegasus PIV laser Nd:YLF from New Wave Research and two CMOS NanoSense Mk III cameras from Dantec Dynamic A/S. The laser has double head emitting coherent light with wavelength 527 nm by maximal frequency equal to 10 kHz. The pulse energy is optimized for 1 kHz when its value is 10 mJ (corresponding power is 10 W per head). Both cameras with resolution 1280 x 1024 pixels were equipped with Nikon lenses. As shown in figure 4 the multi-level calibration target was designed and 3D printed exclusively for this application. The velocity vector maps with 129 x 110 vectors corresponds to space resolution approx. 1 mm. The water was saturated by a borosilicate silver coated glass particles from Dantec. Diameter of particle is 10 μm with spherical shape and smooth surface. For each measured flow ratio totally 1636 snapshots were acquired with record length $t = 3.27$ s.

3.3. Measurements uncertainties
Several uncertainties were accounted for both PIV and high speed camera recording. Regarding the PIV the positioning uncertainty of calibration target was lowered to minimum by using the calibration target with outer dimensions equal to inner dimensions of diffuser cone. The verticality of target placed in diffuser was checked by micro spirit level. The Scheinpflug lens mounting was used for PIV cameras, however, the angle between lenses axes and the diffuser outer surface was far from to be perpendicular, as recommended in similar situation [22]. This configuration has been dictated by spatial restrictions. The uncertainty of flow rate plays significant role since the ratio between axial and tangential inflow was set accordingly. The flow rate uncertainty was quantified as combination of flow meter accuracy and actual measured flow rate. For nominal flow rate $Q_n = 10$ l/s the maximal uncertainty 0.05 l/s was estimated. The pressure sensor behind test section was used to measure pressure level and consequently evaluate Thoma cavitation number σ as further described in equation (2). The measuring range of this sensor is $0 - 6$ bars with uncertainty 0.00625 bars.

30th IAHR Symposium on Hydraulic Machinery and Systems

IOP Conf. Series: Earth and Environmental Science **774** (2021) 012085

IOP Publishing

doi:10.1088/1755-1315/774/1/012085

4. Proper orthogonal decomposition

The proper orthogonal decomposition (POD) was introduced to the field of fluid mechanics in 1967 by Lumley [23] as a method for identification of coherent structures. POD can be used to analyze experimental and numerical data that are applied to scalar or vector functions.

Let $u = f(\mathbf{x}, t_k)$ be a variable dependent on spatial coordinates $\mathbf{x} = (x, y, z)$ and discrete time t_k. Given a set of data can be expressed using POD as a set of orthogonal spatial basis functions $\phi_i^j(\mathbf{x})$ (spatial modes) and temporal functions $a_j(t_k)$ (temporal modes), where $i = 1, 2, ..., N$ (N is number of grid points), $k = 1, 2, ..., M$ (M is number of snapshots) and $j = 1, 2, ..., L$ (L is number of summed modes and $L \leq M$). Accordingly, the approximation of the data set in the first L modes can be written in terms of the spatial and temporal functions as follows:

$$u_i(\mathbf{x}, t_k) = \sum_{i=1}^{L} \phi_i^j(\mathbf{x}) a_j(t_k) \tag{1}$$

where $L \leq M$ has the largest mean square projection. In the method of snapshots, the general $N \times N$ eigenvalue problem is reduced to an $M \times M$ eigenvalue problem. This solution enables a substantial reduction in computational effort when the number of grid points N significantly exceeds the number of dataset snapshots M. The inner products of all pairs of the sampled fields, i.e., the snapshots, are the temporal correlation matrix $\mathbf{C}(t_k', t_k)$ used as the kernel and defined in discrete form as $\mathbf{C}(t_k', t_k) = M^{-1} \mathbf{U}(\mathbf{x}, t_k') \mathbf{U}(\mathbf{x}, t_k)$, where $\mathbf{U}(\mathbf{x}, t_k)$ is the data matrix where the columns are snapshots. On solving the eigenvalue problem of the form $\mathbf{CA} = \lambda \mathbf{A}$ we obtain the matrix of eigenvectors $\mathbf{A}$, where a_j is the jth column, and corresponding eigenvalues λ_j. If u is velocity (obtained by PIV for example), we are minimizing the residual kinetic energy. For this reason, POD is often referred to as the energetically optimal method. More details on the computation of POD modes from discrete data might be found in [24, 25].

In this work POD was applied on measured flow fields by PIV to identify the main dynamics features of generated swirling flow.

5. Results

Using the high speed camera the spatial shape of cavitating vortex was recorded for different flow ratios. For each flow ratio four distinct snapshots are shown in figures 5 - 10. It is obvious that the vortex shape is inconsistent in time and the spatial shape changes significantly with various flow ratios. While at flow ratios with low tangential inflow (figures 5 - 7) the well developed spiral vortex appears, at flow ratios with high tangential inflow (figures 9 - 10) the upper part of vortex is formed by large amount of cavitation. Moreover in regimes close to flow ratio 50:50 (axial to tangential) it was observed that the vortex spiral grows and collapses periodically. Such behavior is accompanied by creation of vortex ring and is documented in previous study [19].

In order to quantitatively describe the flow conditions with cavitating vortex, Thoma cavitation number σ was calculated as:

$$\sigma = \frac{p - p_v}{\frac{1}{2} \rho v_0^2} \tag{2}$$

where p is static pressure measured behind the diffuser section, p_v is pressure of saturated vapour, ρ is water density and v_0 is mean velocity in diffuser throat area. Consequently, for visualized cavitating vortex depicted in figures 5 - 10 average value of $\sigma = 7.9$.
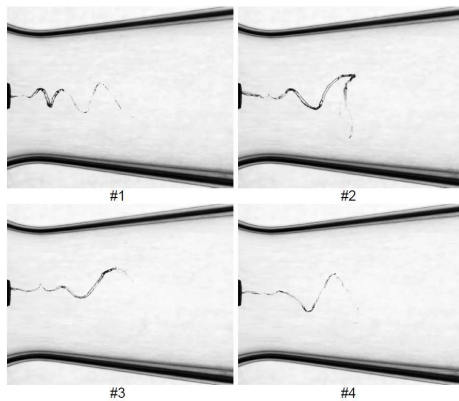
Figure 5. Cavitating vortex at 55:45 of axial to tangential flow ratio, $\sigma = 7.82$, $S = 0.21$.
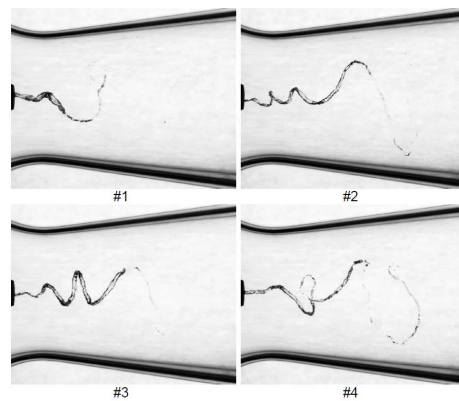

Figure 6. Cavitating vortex at 50:50 of axial to tangential flow ratio, $\sigma = 7.85$, $S = 0.26$.
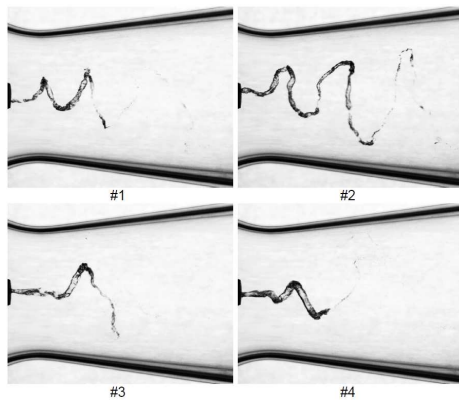

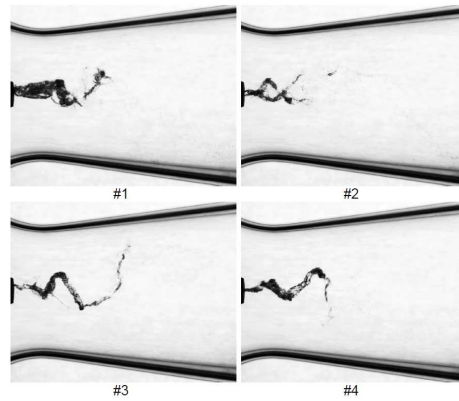**Figure 7.** Cavitating vortex at 45:55 of axial to tangential flow ratio, $\sigma = 7.88$, $S = 0.32$.

Figure 8. Cavitating vortex at 40:60 of axial to tangential flow ratio, $\sigma = 7.91$, $S = 0.38$.
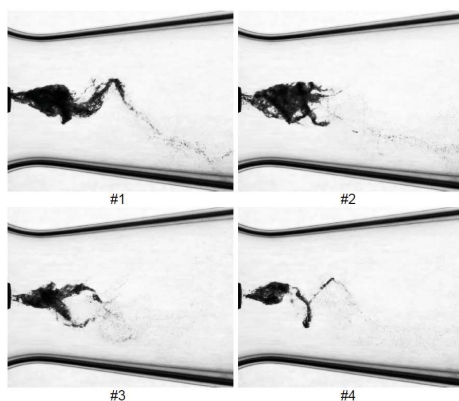

Figure 9. Cavitating vortex at 35:65 of axial to tangential flow ratio, $\sigma = 7.96$, $S = 0.45$.
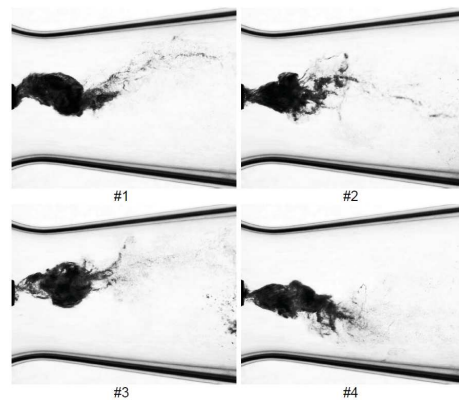

Figure 10. Cavitating vortex at 30:70 of axial to tangential flow ratio, $\sigma = 8.00$, $S = 0.52$.

The swirling flow magnitude as a ratio between axial to tangential inflow is determined by the swirl number S. It is a dimensionless parameter commonly used to characterize a swirling flow at high Reynolds numbers. When the critical swirl number is reached the vortex breakdown occurs. The widely used swirl number is defined as $S = \frac{\int uwrdS}{R\int u^2 dS}$ where u is the time-averaged axial velocity, w is the time-averaged tangential velocity, r is the radial coordinate and R is reference radius. In our case the swirl number is evaluated on single line from planar PIV grid (as shown in figure 11), thus the equation might be modified as

$$S = \frac{\int_0^R uwrdr}{R\int_0^R u^2 dr} \qquad (3)$$

This evaluation line is situated in throat of diffuser, close to the border of PIV grid and contains only 39 points with valid PIV vectors. Together with relatively short record length of $t = 3.27$ s the exact value of swirl number might not be precisely estimated. This was particularly case of flow ratio 30:70 with nominal flow rate $Q = 10$ l/s. This regime was at the limit of cavitation occurrence which could distort PIV record. That was reason why the larger portion of tangential inflow was measured for $Q = 5$ l/s. As shown in figure 12 the swirl number gradually increases as the portion of tangential inflow increases. The black dotted line denotes the trend line estimated as a combination of both data sets.
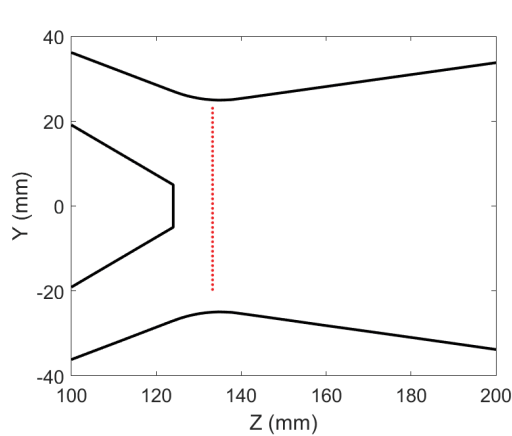

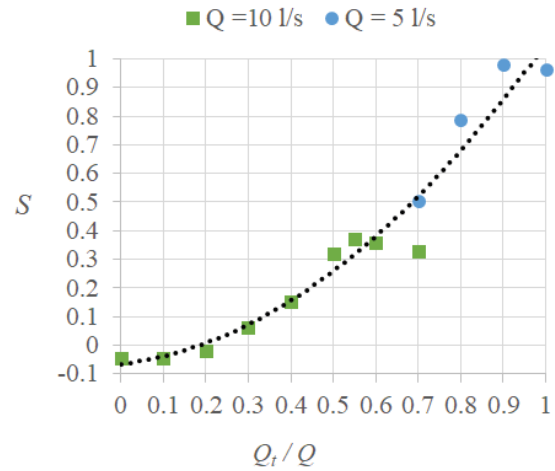**Figure 11.** Line for evaluation of swirl number.

Figure 12. Swirl number evolution.

Figure 13 shows contours of axial velocity v_{ax} for four different flow ratios. The red line marks the border of backflow region where $v_{ax} < 0$. It is obvious that the size of backflow region increases and changes shape with variation of flow ratio. Comparing these results with figures 5 - 10 it is possible to conclude the influence on spatial shape of cavitating vortex. In order to identify the region of largest velocity fluctuations the root mean square of velocity magnitude was calculated as follows

$$RMS_v = \sqrt{\frac{1}{N}\sum_{i=1}^{N}(v_i - v_{avg})^2} \qquad (4)$$

where v_i is recorded sample of velocity magnitude, v_{avg} is average from whole record. Results are depicted in figure 14.
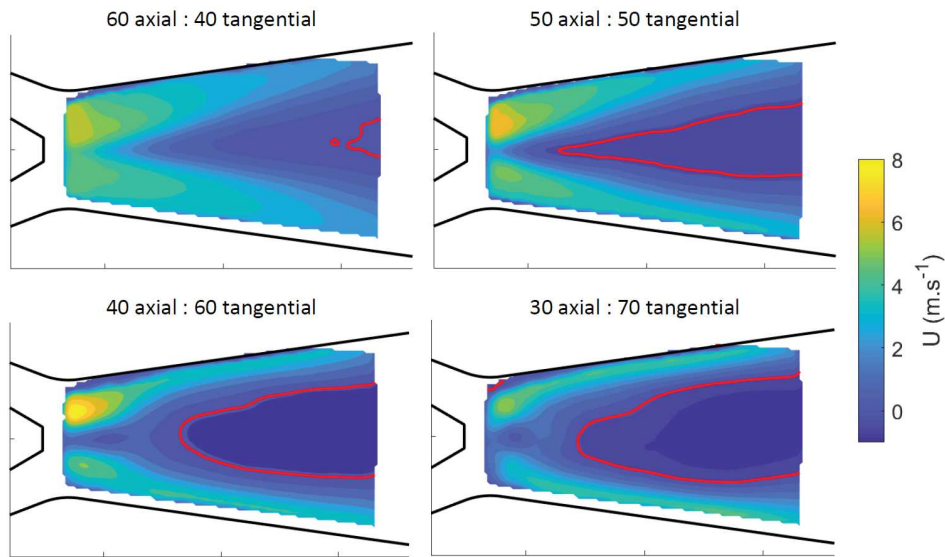
Figure 13. Contours of axial velocity (red lines separate the backflow region).

While at flow regimes 60:40 and 50:50 (axial to tangential) the regions of largest velocity fluctuations form the conical-like shape leading from the end of hub, at regimes with higher portion of tangential inflow the largest velocity fluctuations are found in the outer periphery of diffuser throat. This redistribution might point to the significant change in vortex spatial shape.
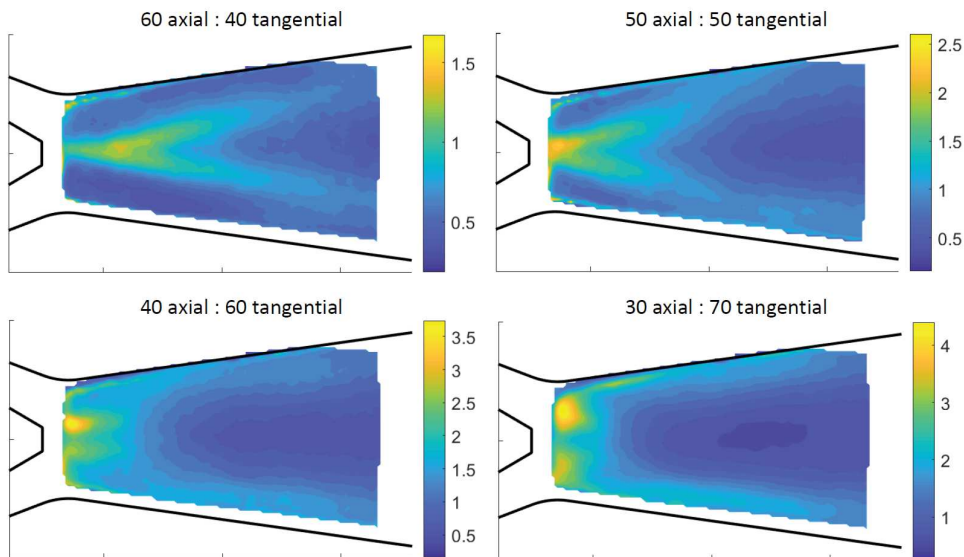

Figure 14. Contours of velocity magnitude root means square RMS_v.

5.1. Modal decomposition of PIV data

POD was primarily applied to the field of radial velocity v_{rad}. It is known that even small instability is well recognizable in a field of v_{rad} and thus is suitable for such analysis. Figure 16 shows variation of radial velocity modes for four different flow ratios. Spatial shape in form of contours plot, relevant modal frequency f and percentage contribution to the overall energy spectra are presented for the first four dominant modes $\#1 - \#4$.

The change in flow ratio brings the variation in spatial modes as well as change of modal frequency and percentage contribution. While at flow ratio 60:40 (axial to tangential) the mode #1 contributes to the overall energy spectra by 8.7 %, at flow ratio 30:70 (axial to tangential) it is already more than three times higher (31.4%). As shown in figure 18 the frequency of mode #1 increases linearly with increase of tangential inflow and denotes the dominant frequency of generated vortex. One can see that frequency of mode #1 and #2 is identical and percentage contribution is very similar. If we plot temporal mode a_1 against a_2 we will get so called phase portrait as depicted in figure 15. Circular shape denotes $\pi/2$ phase shift between these two modes #1 and #2, which means that those two POD modes create one Fourier mode in form of traveling wave .
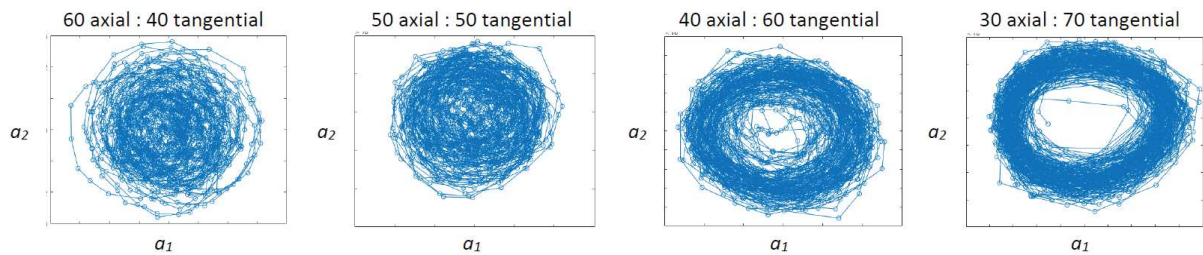

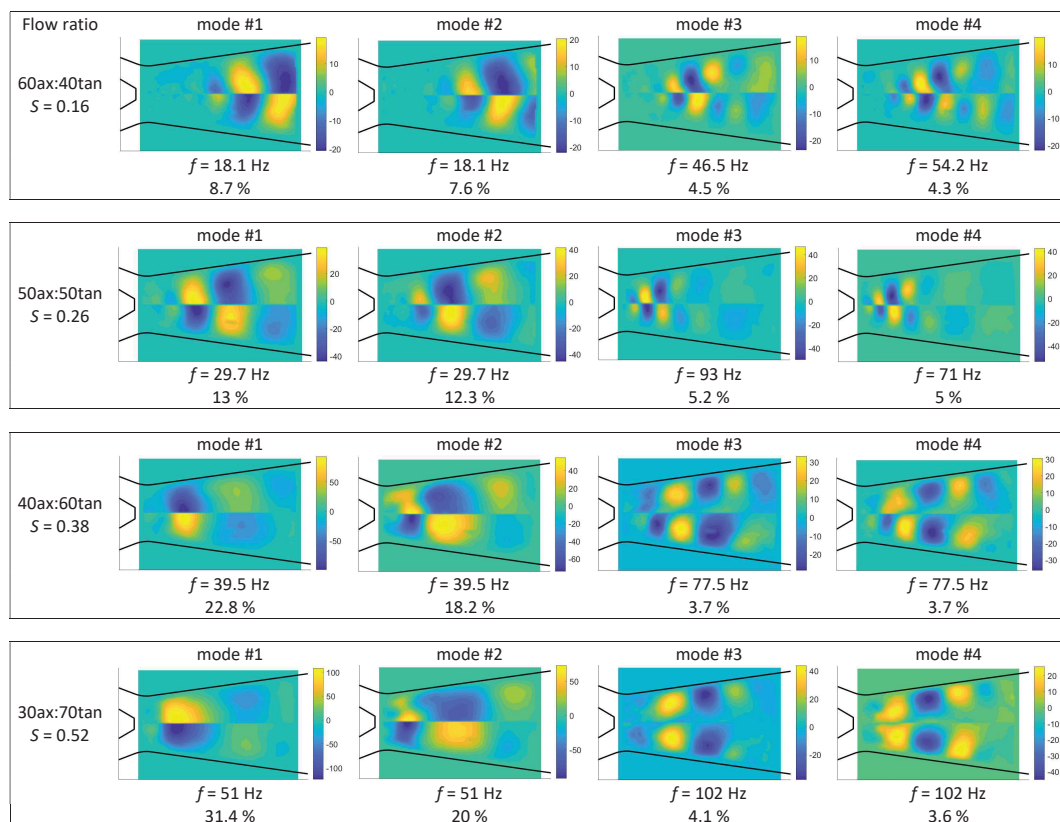**Figure 15.** Phase portraits of temporal modes a_1 and a_2

Figure 16. Variation of radial velocity modes

From spatial shapes, identical modal frequency, similar percentage contribution and phase portraits we can conclude, that modes #1 and #2 create a complex Fourier mode [26]. These modes appear especially in case that POD is applied on flow in axi-symmetric domain, e.g. vortex rope in draft tube of hydraulic turbine [27, 28].

Different situation applies for modes #3 and #4. Their frequency sometimes varies and it is not always dominant in frequency spectra as for modes #1 and #2. Percentage contribution is also much smaller as shown in figure 17 and remains around same magnitude. It is important to highlight that the spatial shape of modes #3 and #4 at flow ratios 40:60 and 30:70 is different to all others pointing on some longitudinal wave propagation.

Finally, the instability of vortex breakdown starts to appear somewhere between flow ratio 80:20 and 70:30 (axial to tangential inflow). This might be well identified from figure 18 where the frequency of mode #1 is plotted with lowest value at $Q_t/Q = 0.3$.
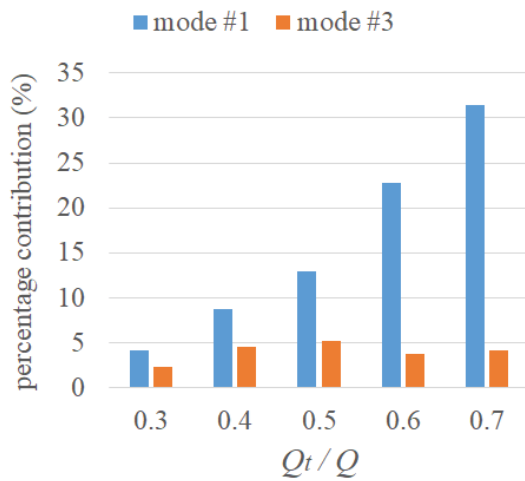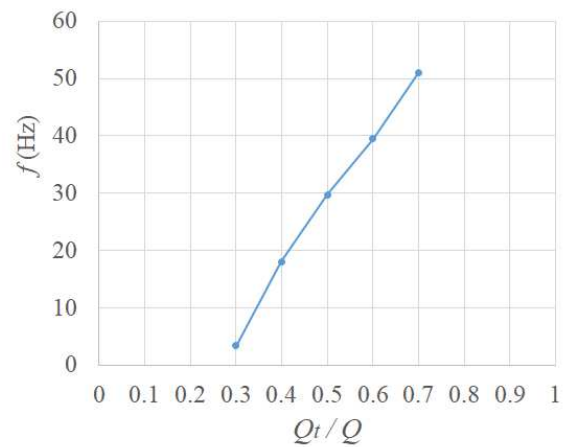

Figure 17. Mode's percentage contribution.

Figure 18. Frequency of mode #1.

6. Conclusions

The unsteady spiral vortex structure was studied using simple device of swirl generator apparatus. The spatial shape of generated vortex structure changes according to variation of swirl number S. From video record of cavitating vortex it might be concluded, that type of vortex breakdown is dependent on magnitude of swirl number S. While for interval $0.2 < S < 0.4$ the spiral form of vortex breakdown develops, for $S > 0.4$ the "wasp-nest-like" shape with large amount of cavitation region just under the hub and short spiral tail is formed. This fact is reflected in modal decomposition of radial velocity field. At flow ratios 40:60 and 30:70 the spatial shape of modes #3 and #4 reveal longitudinal wave with frequency twice higher than for modes #1 and #2.

By swirl number estimation and POD analysis it was possible to identify the combination of axial to tangential inflow when the vortex breakdown starts to develop. Such a ratio is approximately 75:25 (axial to tangential inflow) with estimated swirl number $S = 0.04$. Approximately at this flow ratio the frequency of mode 1 is becoming nonzero, thus the vortex breakdown instability emerges.

In future work we will concentrate on CFD simulation employing scale resolving turbulence model and presented experimental results will be used for verification.

Acknowledgments

References

[1] Frunzăverde D, Muntean S, Mărginean G, Câmpian V, Marşavina L, Terzi R and Şerban V 2010 *IOP Conference Series: Earth and Environmental Science* **12** 1–10

[2] Rheingans W J 1940 *Transactions of the ASME* **62** 1–14

[3] Silva P C O, Nicolet C, Grillot P, Drommi J L and Kawkabani B 2017 *IEEE Transactions on Industry Applications* **53** 3345–3354

[4] Valentín D, Presas A, Egusquiza E, Valero C, Egusquiza M and Bossio M 2017 *Energies* **10**

[5] Dörfler P, Sick M and Coutu A 2013 *Flow-Induced Pulsation and Vibration in Hydroelectric Machinery: Engineer's Guidebook for Planning, Design and Troubleshooting* (London: Springer London) pp 1–31

[6] Susan-Resiga R, Muntean S, Tanasa C and Bosioc A 2008 *4th German—Romanian Workshop on Turbomachinery Hydrodynamics* (Stuttgart, Germany) pp 1 – 16

[7] Gramlich M 2012 *Numerical Investigations of the Unsteady Flow in the Stuttgart Swirl Generator with OpenFOAM* Master's thesis Chalmers University of Technology Gothenburg, Sweden

[8] Bosioc A I, Susan-Resiga R, Muntean S and Tanasa C 2012 *J. Fluids Eng.* **134** 11

[9] Štefan D, Rudolf P, Muntean S and Susan-Resiga R 2013 *Engineering MECHANICS* **20** 339–353

[10] Javadi A and Nilsson H 2017 *Engineering Applications of Computational Fluid Mechanics* **11** 30–41

[11] Litvinov I, Shtork S, Gorelikov E, Mitryakov A and Hanjalic K 2018 *Experimental Thermal and Fluid Science* **91** 410 – 422

[12] Tsoy M A, Skripkin S G and Shtork S I 2015 *2015 5th International Youth Conference on Energy (IYCE)* pp 1–5

[13] Skripkin S, Tsoy M, Shtork S and Hanjalić K 2016 *Journal of Hydraulic Research* **54** 450–460

[14] Müller A, Yamamoto K, Alligné S, Yonezawa K, Tsujimoto Y and F F A 2015 *J. Fluids Eng.* **138** 8

[15] Stuparu A and Susan-Resiga R 2015 *6th IAHR International Meeting of the Workgroup on Cavitation and Dynamic Problems in Hydraulic Machinery and Systems* (Ljubljana, Slovenia) p 8

[16] Alekseenko S V, Kuibin P A, Shtork S I, Skripkin S G, Sonin V I, Tsoy M A and Ustimenko A S 2016 *IOP Conference Series: Earth and Environmental Science* **49** 1–7

[17] Skripkin S G, Tsoy M A, Kuibin P A and Shtork S I 2017 *Journal of Fluids Engineering* **139**

[18] Skripkin S, Tsoy M, Kuibin P and Shtork S 2019 *Experimental Thermal and Fluid Science* **100** 349 – 359

[19] Štefan D, Rudolf P, Hudec M, Uruba V, Procházka P and Urban O 2019 *IOP Conference Series: Earth and Environmental Science* **405** 012033

[20] Pochylý F, Urban O and Fialová S 2019 *IOP Conference Series: Earth and Environmental Science* **240** 072026

[21] Urban O and Rudolf P 2019 *IOP Conference Series: Earth and Environmental Science* **405** 012034

[22] Raffel M, Willert C E, Scarano F, Kähler C, Wereley S T and Kompenhans J 2018 *Particle Image Velocimetry, A Practical Guide* (Springer International Publishing) p 669

[23] Lumley J L 1967 *Atmospheric Turbulence and Wave Propagation* ed Yaglom A M and Tatarski V I (Moscow: Nauka) pp 166–178

[24] Berkooz G, Holmes P and Lumley J L 1993 *Annual Review of Fluid Mechanics* **25** 539–575

[25] Štefan D, Rudolf P, Muntean S and Susan-Resiga R 2017 *Journal of Fluids Engineering* **139** ISSN 0098-2202

[26] Citriniti J H and George W K 2000 *Journal of Fluid Mechanics* **418** 137–166

[27] Rudolf P and Štefan D 2012 *IOP Conference Series: Earth and Environmental Science* **15** 062008

[28] Stefan D and Rudolf P 2015 *Journal of Physics: Conference Series* **579** 012002